S^{2-} doping inducing self-adapting dual anion defects in ZnSn(OH)$_6$ for highly efficient photoactivity

Bangfu Chen [a], Zeyong Meng [a], Ping Ouyang [a], Youyu Duan [b,*], Yuhan Li [a,*], Wanjun Wang [c], Fan Dong [a]

[a] Engineering Research Center for Waste Oil Recovery Technology and Equipment, Ministry of Education, Chongqing Key Laboratory of Catalysis and New Environmental Materials, Chongqing Technology and Business University, Chongqing 400067, China
[b] College of Physics and Institute of Advanced Interdisciplinary Studies, Chongqing University, Chongqing 401331, China
[c] Guangdong Key Laboratory of Environmental Catalysis and Health Risk Control, Guangzhou Key Laboratory Environmental Catalysis and Pollution Control, School of Environmental Science and Engineering, Institute of Environmental Health and Pollution Control, Guangdong University of Technology, Guangzhou 510006, China

ARTICLE INFO

ABSTRACT

The S^{2-} doping and oxygen vacancies (OVs) co-modified ZnSn(OH)$_6$ (ZHS) were fabricated by the microwave method. Due to the synergistic effects of S^{2-} doping and OVs in ZHS, the removal rates of toluene and nitric oxide reached 92.5 % and 49.8 %, respectively. Experimental and theoretical results (DFT) show that the improved photoactivity can stem from: 1) the alteration of O 2p band center position. S^{2-} doping causes the O 2p band center to shift upward relative to the Fermi level, reducing the formation energy of OVs; 2) the change of the local electron distribution. A rapid charge transfer channel was formed between S^{2-} and adjacent OVs; 3) abundant active sites. The activation of small molecules on the photocatalyst surface were promoted and produced rich active free radicals. Thus, the construction of dual anion defects modified photocatalyst offers a simple strategy for the design of highly efficient photocatalyst for air pollution control.

1. Introduction

As a typical representative of highly toxic benzene-based VOCs, toluene (C$_7$H$_8$) is of practical significance as a model molecule to study the removal of VOCs [1]. In comparison to other technologies for eliminating C$_7$H$_8$, photo-oxidation can easily generate hydroxyl radicals (·OH) with strong oxidizing ability and other reactive oxygen species (ROSs), leading to subsequent ring-opening followed by chain oxidation reaction to achieve deep mineralization under green and mild conditions [2–4]. Unfortunately, the advance on the photocatalytic deep mineralization of C$_7$H$_8$ to CO$_2$ and H$_2$O is hampered by the following four bottlenecks: 1) Poor adsorption. The adsorption of C$_7$H$_8$ on the photocatalyst surface is weak, and the resulting cresol and resorcinol intermediate further hinder the adsorption of C$_7$H$_8$ [5]. 2) Inefficient carrier dynamics. Photogenerated carriers cannot efficiently migrate to the surface of the material, and it is difficult to further react with O$_2$ and H$_2$O to form ROSs, such as ·O$_2^-$ and ·OH, which hinder the final redox reaction [6]. 3) Difficult to activate the reaction. C$_7$H$_8$ has a stable benzene ring structure and C(sp^3)-H bond. The breakup of the aromatic ring (147 kcal·mol^{-1}) and activation of the C(sp^3)-H bond (88.5

kcal·mol^{-1}) require high dissociation energy, thereby the transformation usually requires harsh conditions and strong oxidants [3,7–9]. 4) The formation of multiple toxic by-products. Product selectivity is difficult to control, resulting in oxidation reactions to produce more hypertoxic intermediates such as ketones and aldehydes and large amounts of ozone [10–12]. Meanwhile, excessive deposition of tar or stable carbonaceous byproducts on the surface of the photocatalyst, which reduces the active sites of the photocatalyst and greatly affects the activity as well stability [13,14]. Hence, the development of efficient photocatalysts to cope with challenging reactions (effective adsorption and activation of C$_7$H$_8$), and achieve the deep mineralization of C$_7$H$_8$ to CO$_2$ and H$_2$O, which has potential applications in protecting human health and alleviating growing environmental problems.

ZnSn(OH)$_6$ (ZHS), as a typical perovskite-based composite metal hydroxide, and its metal ions form octahedral coordination with -OH to form Sn(OH)$_6$ and Zn(OH)$_6$ polyhedra, which are interlinked with each other through the O corners to form a face-centered cubic crystal structure [15]. In addition, there is a strong covalent bond between Zn and Sn in the crystal structure, and charge can be transferred between the covalent bonds. Meanwhile, the -OH groups on the surface can

---

accessibly accept photogenerated holes to form hydroxyl radicals (E_φ(-OH/·OH) = 1.23 V versus. NHE.) [16]. Therefore, due to its excellent physical and chemical properties and environmentally friendly features, it is considered a promising photocatalyst. According to previous reports, it is easy to improve the photocatalytic performance of ZHS through modification strategies such as crystal facet control [17], element doping [18] and heterojunction establishment [19]. However, several limitations of the existing methods hinder their popularization and application. This is attributed to three major reasons: 1) The modification reagent is expensive and has a deficiency in economic performance [20]; 2) Synthetic scheme for complex (two-step synthesis even three-step synthesis), the preparation process is long and difficult to mass production [16,21]; 3) Most modification strategies inevitably introduce Zn or Sn oxides into the ZHS system to influence photogenerated carrier transfer by constructing heterojunctions [14]. However, it is difficult to effectively separate electron-hole pairs with high redox potential by traditional type II and Z heterojunctions [22–24].

To bridge this gap, the key to improve the photocatalytic performance of ZHS is to find an effective modification strategy to better the optical and photoelectric properties of ZHS, such as light absorption capacity, photogenerated carrier separation efficiency and the dynamics of carrier transfer. It is well known that the introduction of impurity ions and oxygen vacancies (OVs) can affect the physicochemical properties of the photocatalytic material such as local atomic arrangement, electronic structure, charge transfer pathways and so on [5,25]. Doping of elements is generally capable of narrowing the bandgap and introducing doping levels in the bandgap of photocatalyst to simultaneously enhance the optical absorption and photoexcited charge separation [26,27]. OVs as the prevalent surface anion defects, which could act as electron traps and active sites to promote the efficient separation and migration of photogenerated charge carriers, and hinder the recombination rate of charge carriers [25,28,29]. More remarkably, the introduction of the S element can promote the formation of OVs [30], mediate the band structure, improve the concentration of carrier, and provide sufficient sites for the adsorption and activation of H_2O/O_2 molecules, thus giving rise to the enhanced photoreactivity [31,32]. As exemplified by Guo et al., they synthesized S-doped $AgFeO_2$ with OVs for photocatalytic reduction of U(VI) in aqueous solutions. The enhanced photoreduction performance of adsorbed U(VI) can be attributed to the unique OVs effect and efficient charge separation [33]. Also, Wang et al. found that the S/OVs co-modified BiOBr nanosheet exhibits a photocatalytic removal rate of 4.9- and 18.0-times higher than that of pristine ultrathin BiOBr and S-doped BiOBr, respectively. The photoactivity improvement can be attributed to the extended light absorption capacity and efficient charge separation via the synergistic effect between S doping and OVs [34]. Inspired by the above-mentioned works, the construction of dual anion defects (doping and OVs) by simple preparation route is a promising strategy to solve intrinsic ZHS deficiency and improve photocatalytic performance.

In this study, dual anion defects (S^{2-} doping and OVs) modified ZHS was prepared through a simple one-step water-bath microwave method. Detailed characterizations and tests confirm that the S^{2-} doping and OVs in the ZHS nanoparticles can effectively narrow the bandgap, enhance light absorption, and promote electron transfer and inhibit the recombination of electron-hole pairs. Moreover, density functional theory (DFT) calculations and diffuse reflectance infrared Fourier transform spectroscopy (DRIFTS) have also revealed that the construction of dual anion defects enhances the adsorption and activation of small molecules and C_7H_8 in a flow catalytic reaction, thus providing boosted photocatalytic oxidation performance towards C_7H_8 and NO. The present work may offer a new perspective for the ingenious design and synthesis of dual anion defects steered photocatalysts.

2. Experimental section

2.1. Preparation of samples

Stannic chloride ($SnCl_4 \cdot 5\ H_2O$), zinc acetate ($Zn(AC)_2 \cdot 2\ H_2O$), sodium hydroxide (NaOH), thioacetamide (C_2H_5NS) and methylcellulose were purchased from SINOPHARM Chemical Reagent Co. All chemicals were analytical grade and used without further purification. Deionized water with a resistivity (18.2 MΩ·cm) was used during the experimental process.

A series of samples with dual-anionic defects (SZHS-*x*) were synthesized via a water-bath microwave with C_2H_5NS as the source of the S dopant. In the conventional synthesis, 1) 30 mL of deionized water, 2 mL of $Zn(AC)_2 \cdot 2\ H_2O$ (0.5 mol·L^{-1}) and 2 mL of $SnCl_4 \cdot 5\ H_2O$ (0.5 mol·L^{-1}) were added into an Erlenmeyer flask for magnetic stirring. 2) C_2H_5NS with different mass ratios were added into the aforesaid Erlenmeyer flask and stirred for 10 min 3) 2.3 mL of NaOH solution (3 mol·L^{-1}) and 10 mL of methylcellulose (2.8 g·L^{-1}) were dropwise added into the asmentioned mixture and kept stirring for 30 min 4) The stirred solution was transferred into the PTFE liner; the residual solution in the Erlenmeyer flask was washed with 20 mL of deionized water and then transferred to the same PTFE liner. 5) Heating the hydrothermal reactor at 120 ℃ for 1 h in the microwave reactor. After finishing the reaction and cooling the reactor to room temperature, the white precipitate was collected and then washed by three times alternately with deionized water and ethanol, and then dried at 60 ℃ for 12 h. The mass ratios of C_2H_5NS to ZHS were controlled at 0 %, 3 %, 5 %, 7 %, 10 %, 15 %, 20 % and 30 %, and labeled as SZHS, SZHS-3, SZHS-5, SZHS-7, SZHS-10, SZHS-15, SZHS-20 and SZHS-30, respectively.

2.2. Sample characterizations

The phase structure and crystallinity of the samples were investigated by XRD (Bruker D8 Advance) using Cu Kα radiation (40 kV, 40 mA). A scan rate of 5° min^{-1} was applied to record the powder XRD patterns in the 2θ range of 20–80°. X-ray photoelectron spectroscopy (XPS, Thermo Fisher Scientific ESCALAB250Xi, Al KR) was employed to analyze the surface composition, where the C 1 *s* peak at 284.8 eV was used as the calibration peak. Electron paramagnetic resonance (EPR) signals were surveyed at ambient temperature by using a CIQTEK EPR200-Plus spectrometer. Scanning electron microscopy (SEM, JEOL Model JSM-6490, Japan) and transmission electron microscopy (TEM, JEM-2010, Japan) were employed to observe the morphology of asprepared samples. UV–vis diffuse-reflectance spectrometry (DRS) was utilized to analyze the as-made samples using a scan UV–vis spectrophotometer (UV2550, Shimadzu, Japan), 100 % $BaSO_4$ as the reflection sample. Fluorescence spectroscopy (PL, F-7000, HITACHI, Japan) was conducted to investigate the optical properties of the as-formed photocatalysts. The photoelectrochemical performance of as-prepared samples was estimated using a three-electrode collocation (CHI 760E, Chenhua, Shanghai) with the gained electrode, platinum wire, and Ag/AgCl electrode as the counter electrode and reference electrode, respectively. An electrochemical workstation was applied to record the photoelectric current density curves of the photocathodes and Mott-Schottky plots. And electrochemical impedance spectroscopy (EIS) spectra were used to employ a 5-mV amplitude intensity in the frequency range from 10 kHz to 1 Hz. The specific surface area and pore structure measurements of as-made photocatalytic materials were carried out by using an ASAP 2020 system. The DMPO-·O_2^-, DMPO-·OH and DMPO-H_2O_2 were conducted on CIQTEK EPR200-Plus (Hefei) spectrometer equipped with quartz capillary tube under light irradiation, where the 5, 5-dimethyl-1-pyrroline (DMPO, > 99.0%) was chosen as trapping reagent. Furthermore, the EPR spectra of·O_2^- were performed in methanol while the ●OH and H_2O_2 were measured in aqueous solution.

2.3. Evaluation of photocatalytic activity

The photocatalytic activity of the as-prepared samples for C_7H_8 oxidation was measured using a continuous flow system at room temperature (Scheme S1). In detail, 0.1 g of the photocatalyst was evenly loaded on four glass sheets and then placed in the reactor (200 mm × 100 mm × 17 mm) with a quartz glass lid. A 300 W UV high-pressure mercury lamp with a filter (λ = 365 nm) was placed above the reactor vertically as the light source. The gas monitors simultaneously measure the concentrations of C_7H_8, dry air and wet air. The total flow rate was set to 1 L·min^{-1}. Finally, the photocatalytic process was initiated by turning on the lamp after reaching a concentration equilibrium (50 ppm) of C_7H_8. Photoacoustic multi-gas analyzer (GA-SERA ONE, Duke Technology Co. Ltd.) automatically sampled every 2 min and recorded the real-time concentration of C_7H_8 and CO_2. The decomposition ratio (η %) of C_7H_8 was calculated as Eq. (1):

$$\eta = (1 - C/C_0\%) \times 100\ \% \tag{1}$$

Where C and C_0 depict the C_7H_8 concentration in the outlet steam and the feeding stream, respectively.

The C_7H_8 mineralization ratio (M%) was calculated as Eq. (2):

$$M\% = \frac{[CO_2]_{produced}}{[C_7H_8]_{initial} \times 7} \times 100\% \tag{2}$$

Meantime, a continuous flow reactor (L×W×H, 30 cm × 15 cm ×10 cm) equipped with a quartz lid was adopted to evaluate the removal rate of NO with ppb level. See Scheme S2 for details.

2.4. DFT simulations

All the spin-polarized density functional theory (DFT) calculations were carried out in the "Vienna A*b* initio Simulation Package" (VASP 5.4) with the generalized gradient approximation using the Perdew-Burke-Ernzerhof (PBE) exchange and correlation functional [35,36]. The standard pseudopotential (USP) method recommended by the VASP manual was utilized to construct the pseudopotential. The plane wave truncation energy (E_{cut}) was 450 eV, and the ion relaxation convergence standard was $- 0.03$ eV·Å^{-1} [37]. As the computational model, ZHS (220) supercell containing 112 atoms was well established. After the optimal convergence of the system geometry reached the lowest configuration of energy, the subsequent calculation was carried out. A 15 Å vacuum layer was used to simulate the adsorption state of adsorbed small molecules on the catalyst surface, and the underlying atoms were fixed during the structural optimization process of the model.

The formation energy (ΔE_f) of the surface OVs on samples was calculated according to Eq. (1).

$$\Delta E_f = E_{S\text{-slab}}(\text{with OVs}) + E(O) - E_{S\text{-slab}}(\text{without OVs}) \tag{5}$$

Where $E_{S\text{-slab}}$ (with OVs), E(OH) and $E_{S\text{-slab}}$ (without OV) are the total energy of the model with OVs, the energy of the O atom and the total energy of the model without the OVs, respectively.

The adsorption energy (ΔE_{ads}) was calculated as Eq. (2).

$$\Delta E_{ads} = E_{tot} - E_{S\text{-slab}} - E_{mol} \tag{6}$$

Where E_{tot}, $E_{S\text{-slab}}$ and E_{mol} are the total energy of the adsorption composite system, the total energies of SZHS slab models and the adsorbed small molecules, respectively.

2.5. In situ DRIFTS investigation of C_7H_8 or NO photocatalytic oxidation

In-situ DRIFTS measurements of samples were carried out using a TENSOR II FT-IR spectrometer (Bruker) in a continuous flow atmosphere (Scheme S3).

After the sample is pressed, and then placed into the reaction chamber and heated for 30 min (110 °C) in the atmosphere of high-purity helium to remove the H_2O, O_2, CO_2 and other small molecules adsorbed on the surface of the sample. When the temperature dropped to normal temperature, the sample was immediately scanned by infrared spectrum and used as the background baseline (background baseline should be deducted from all test curves). 50 mL·min^{-1} of C_7H_8 and 50 mL·min^{-1} of O_2 are then sent to the reaction chamber. Under the dark condition, samples were adsorbed for 30 min, while the adsorption state of the surface was detected intermittently (the changes of surface functional groups were recorded). Then, the photocatalytic reaction was carried out for 30 min under ultraviolet light irradiation (visible light illumination for NO), and the infrared spectrum within a certain time interval was recorded. The scanning range of the infrared spectrum was 4000–800 cm^{-1}. (Note: the reaction chamber is equipped with two cooling ports to prevent high-temperature damage to the reaction chamber; A ultraviolet and visible light sources are used as the light source for the C_7H_8 and NO photocatalytic reactions, respectively).

3. Results and discussion

3.1. Photocatalytic performance

Initially, C_7H_8 was chosen as the target pollutant to evaluate the photocatalytic performance of the 0.1 g of the as-prepared sample. As shown in Fig. 1a, the removal efficiencies are in the following order: SZHS-30 (1.5 %) < ZHS (6.6 %) < SZHS-20 (24.1 %) < SZHS-15 (42.2 %) < SZHS-10 (86.2 %) < SZHS-3 (90.8 %) < SZHS-5 (91.4 %) < SZHS-7 (92.5 %). Among all samples, SZHS-7 gives 92.5 % removal rate of C_7H_8 and nearly 102.2 % mineralization within 60 min (Fig. 1b), which is better than other samples. The mineralization rate of the photocatalysts is higher than the removal rate, which can be attributed to the degradation of adsorbed C_7H_8 on the surface of photocatalyst [38]. In order to explore the versatility of the samples towards the photocatalytic degradation of gaseous pollutants, the removal of NO under visible light was also conducted. Unexpectedly, the as-formed NO_2 concentration of 0.1 g of SZHS-7 photocatalyst with the best photoactivity (49.8 %) is lower than 7 ppb, which means SZHS-7 can efficiently oxidize NO and positively inhibit the formation of NO_2 (Fig. S1a-b). As reported [39–41], a large amount of the formed NO_2 intermediates is the biggest bottleneck during NO removal process due to the photocatalyst with feeble oxidation capacity. Fortunately, SZHS-7 holds the promise of deep oxidation ability to effectively photo-decompose C_7H_8 and NO.

In addition, it is well known that the photocatalyst's stability is crucial for commercial applications. The cyclic stability of SZHS-7 was investigated by recycling the photocatalytic removal tests, where C_7H_8 and NO removal rates only decline by 8 % and 4.2 % after 300 min and 165 min, respectively (Fig. 1c and Fig. S2). The above results manifest that the as-formed SZHS-7 is highly active and durable for the photocatalytic degradation of C_7H_8 and NO. Comparable to the efficiency for the reported photocatalytic materials as shown in Fig. 1d. The more detailed comparison is summarized in Table S1.

3.2. Morphology and composition analysis

In Fig. 2a, seven major diffraction peaks at 2θ= 19.62∘, 22.72∘, 32.41∘, 40.04∘, 46.64∘, 52.42∘ and 57.72∘ can be observed in the bare ZHS, which correspond to the (111), (200), (220), (222), (400), (420) and (422) crystal faces of cubic perovskite ZnSn(OH)$_6$ (JCPDS 74-1825), respectively [42,43]. Likewise, SZHS-*x* exhibits similar diffraction peaks as compared with ZHS, indicating that S^{2-} doping has no impact on the original crystal structure of the ZHS. However, with the increase of S^{2-} doping, a slight peak shift of (200) and (220) plane to low 2θ could be found in the XRD patterns, as depicted in Fig. S3. This result indicates that S^{2-} might be incorporated into the lattices of ZHS and leads to the deformations of lattices. According to Bragg's law 2dsinθ = nλ, the peak shift to a low angle reflects the lattice expansion caused by the substitution of the S with a big radius for the oxygen (O) with a small radius
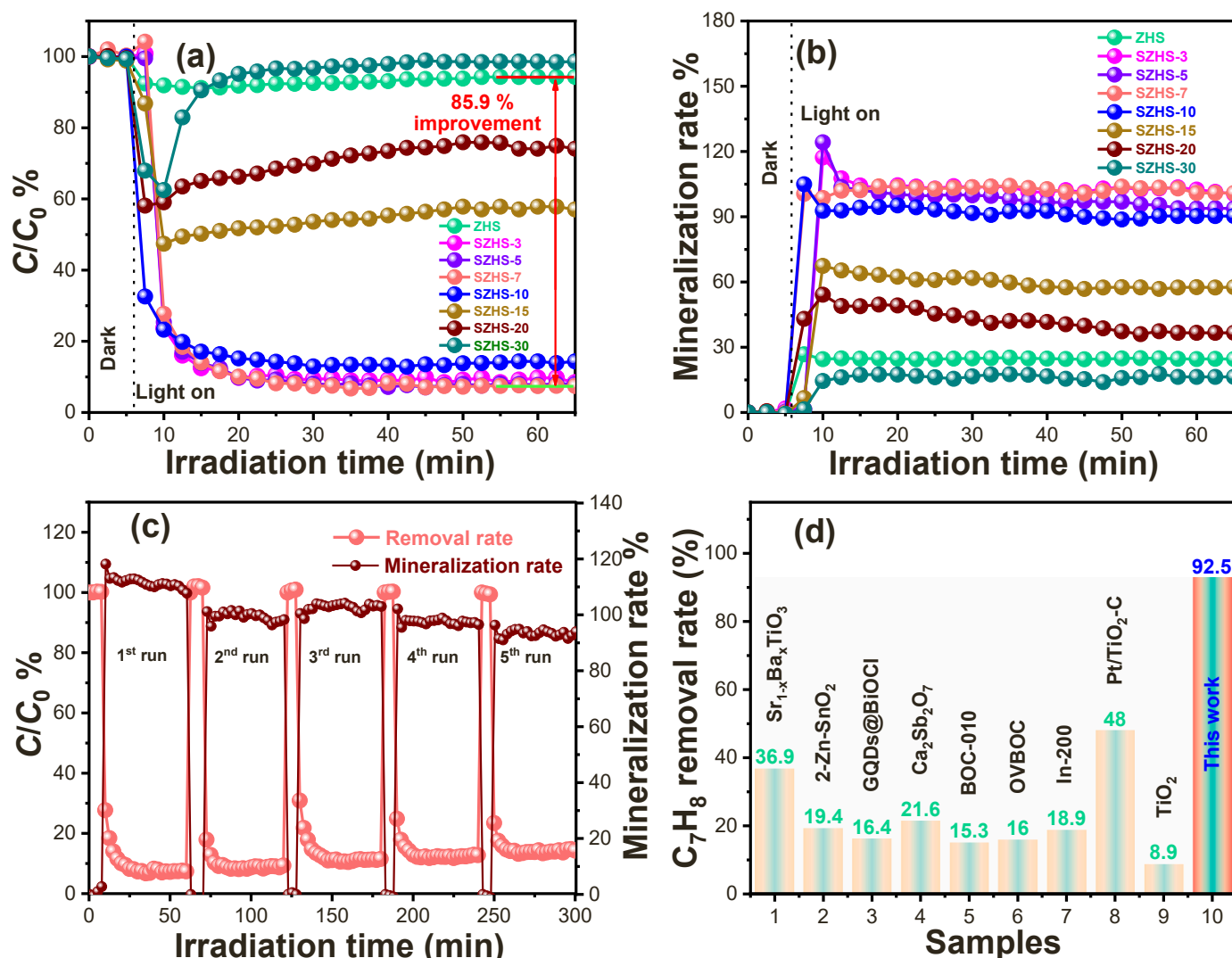
Fig. 1. Photocatalytic C_7H_8 removal efficiency under UV light irradiation (a); and the mineralization for 60 min of C_7H_8 over the as-prepared photocatalysts under UV light irradiation (b); Five recycling measurements over SZHS-7 for photooxidation of C_7H_8 for 300 min (c); and comparison of photocatalytic degradation performance for C_7H_8 of various photocatalysts in the continuous flow reactor (0.1 g of sample) (d).

[44,45].

The morphology, structure and size of the ZHS and SZHS-7 were investigated by SEM and TEM images. As shown in Fig. 2b and Fig. S4a, the SEM images of ZHS and SZHS-7 present a uniform and cubic-like morphology with a length of 200–500 nm, indicating the S^{2-} doping does not cause variation of the basic morphology. In addition, the HRTEM images of ZHS and SZHS-7 (Fig. 2c and Fig. S4b) exhibit well-defined lattice fringes with an inter-planar distance of 0.393 nm, corresponding to the crystal plane of ZHS (200), which is consistent with the previous reports on ZHS [19,42]. N_2 adsorption-desorption measurements suggest that the ZHS and SZHS-7 possess similar specific surface area and pore size (Fig. S5), as summarized in Table S2, which suggests that the difference in photocatalytic activity is not directly related to the specific area or pore size.

Furthermore, the existence of the S dopants was confirmed by the XPS results. In the XPS survey spectra of bare ZHS and SZHS-7 samples (Fig. S6a), the presence of S $2p$ peak only in the spectrum of SZHS-7 further indicates the successful doping of S in ZHS. The low-intensity peaks center at 161.6 and 163.8 eV, corresponding to S $2p_{3/2}$ and S $2p_{1/2}$ (Fig. 2d) of S^{2-}, respectively [33,46]. The peaks located at 1021.8 and 1044.8 eV (Fig. S6b), which assign to Zn $2p_{3/2}$ and Zn $2p_{1/2}$ of the Zn^{2+}, respectively [47]. Meantime, the strong peaks with the binding

energy of 486.8 and 495.3 eV in Fig. 2e can be ascribed to Sn $3d_{5/2}$ and Sn $3d_{3/2}$ of the Sn^{4+} state, respectively [16,48]. It's worth noting that the binding energies of the Sn $3d$ of SZHS-7 shift 0.1 eV towards the direction of high ones, which can be attributed to the high electron-attracting effect caused by the OVs on the Sn atoms surface [28]. And then we can determine whether the O^{2-} site locates at -Sn-O-H is preferred to the substitutional doping of S^{2-}. Visibly, the peaks center at 532.4, 531.6 and 530.5 eV can be assigned to the adsorbed OH^- oxygen state, the oxygen atoms near the oxygen vacancies and lattice oxygen (-Sn/Zn-OH), respectively [16,49,50] (Fig. 2f). The larger area percentage of the peak at ~531.6 eV in SZHS-7 suggests that the formation of OVs in SZHS-7 as a result of the after S^{2-} doping. As such, this result voices that S^{2-} ions with the same valence state can lead to geometric distortion and successfully substitute the O^{2-} ions in the lattice. Besides, solid-state EPR spectra were also recorded to demonstrate the existence of the OVs (Fig. 2g). SZHS-7 emerges a significantly higher EPR signal peak at g= 2.003 as compared with ZHS, which can be attributed to the presence of OVs due to the S^{2-} doping in SZHS-7 [51]. In addition, an extra signal with a g= 2.06 emerges, which should be assigned as Sn^{3+} with the escape of lattice oxygen on the surface of the SZHS-7. In order to further understand the relationship between the introduction of S^{2-} doping and the formation of OVs, DFT calculations were performed to
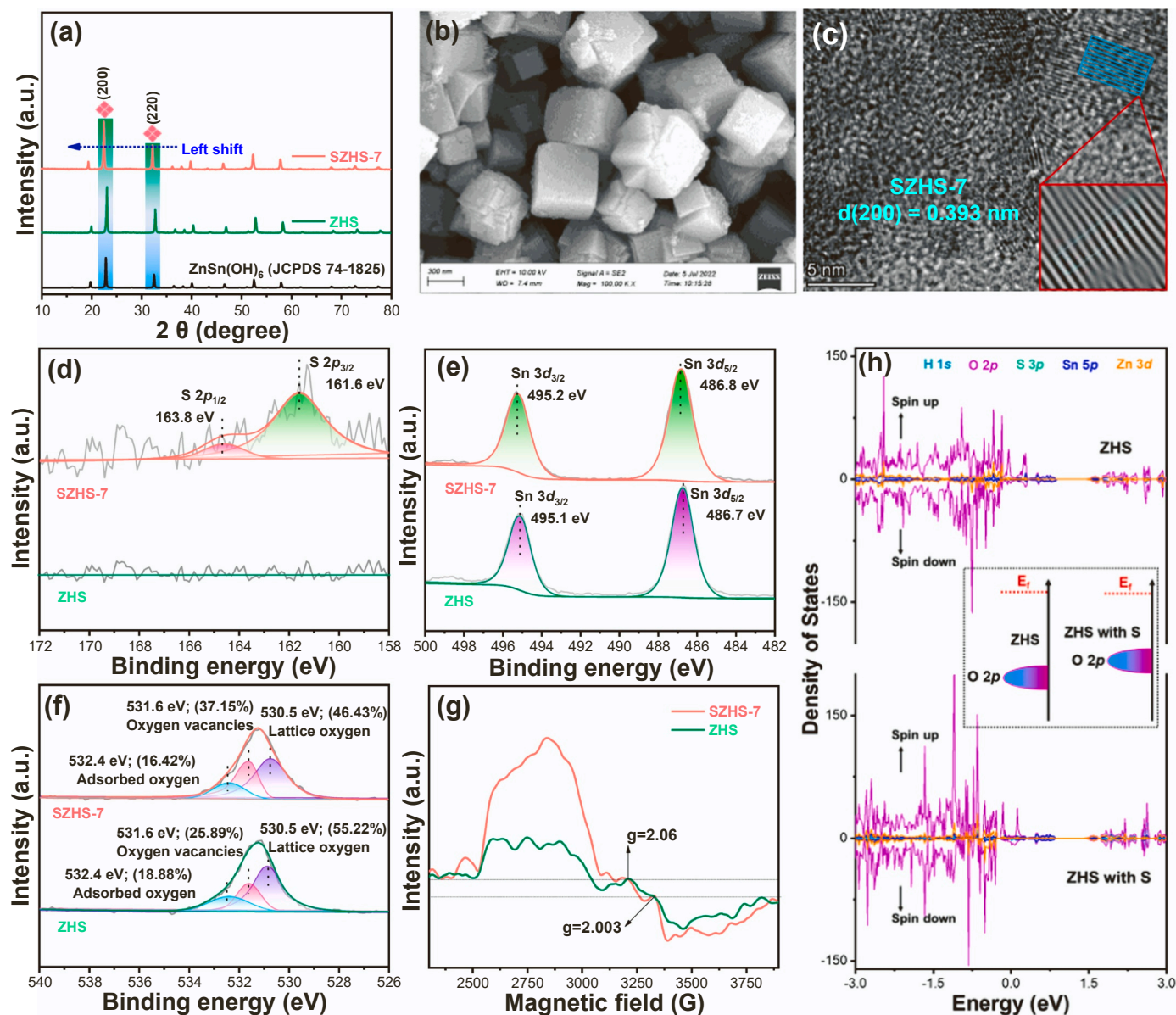
Fig. 2. XRD patterns of the ZHS and SZHS-7 (a); TEM (b) and HRTEM images (c) of SZHS-7; High-resolution XPS spectra of ZHS and SZHS-7: S 1 *s* (d), Sn 3*d* (e), O 1 *s* (f); The EPR spectra of ZHS and SZHS-7 (g); Density of states of the H 1 *s*, O 2*p*, S 3*p*, Sn 5*p* and Zn 3*d* states for ZHS without and with S^{2-} doping (h).

study the changes in the central position of the O 2*p* band induced by S^{2-} doping. The density of states of H 1 *s*, O 2*p*, S 3*p*, Sn 5*p* and Zn 3*d* orbitals with and without surface S^{2-} doping are shown in Fig. 2h. After S^{2-} doping is introduced, the O 2*p* band center of the ZHS moves upward relative to the Fermi level, indicating that the lattice stability of transition metal oxides becomes worse, which is conducive to the formation of OVs [52,53]. Simultaneously, to investigate the influence of S^{2-} doping on the formation of OVs over ZHS with exposed {200} facets, we performed first-principles calculations of two models, i.e., ZHS with OVs (ZHS-OVs) and SZHS with OVs (SZHS-OVs) (Fig. S7). The formation energy for ZHS-OVs is higher than that for SZHS-OVs. And most importantly, we compared the OVs formation energies at different sites of SZHS, Site-1 (Fig. S7b, E_f=1.50 eV) is lower than that Site-2 (Fig. S7c, E_f=1.78 eV). Obviously, the S^{2-} doping promotes the formation of surface OVs at adjacent Sn and is thermodynamically favorable, which is consistent with the XRD, XPS and EPR results.

3.3. Photo(electro)chemical properties and band structures

In order to explore the roles of the dual anion defects in the enhancement of SZHS-7 C$_7$H$_8$ photooxidation activity, the photo(electro)chemical properties and band structure were explored accordingly. The optical absorption ability of the as-obtained samples was evaluated by UV–vis DRS spectra. As shown in Fig. 3a, the absorption edge of pristine ZHS locates at around ~327 nm. Upon S^{2-} doping, the absorption spectra of the SZHS-*x* samples show a redshift, indicative of an extended light absorption range after the introduction of S^{2-} doping and OVs (Fig. S8a). Meanwhile, the bandgaps of ZHS and SZHS-7 were determined from the transformed Kubelka-Munk function [54] and as shown in Fig. 3b. Notably, with the increase of S^{2-} doping, the bandgaps decline from 3.25 eV for ZHS to 2.48 eV for SZHS-7 (Fig. S8b). Furthermore, the Mott-Schottky was employed to measure the electrochemical flat-band potentials (E_{fb}). As depicted in Figs. 3c and 3d, the flat band potential of ZHS and SZHS-7 is determined to be − 0.78 V and − 0.65 V (vs. Ag/AgCl, pH=7), respectively, and the corresponding estimated CB positions are − 0.55 V and − 0.42 V (vs. NHE, pH=7),
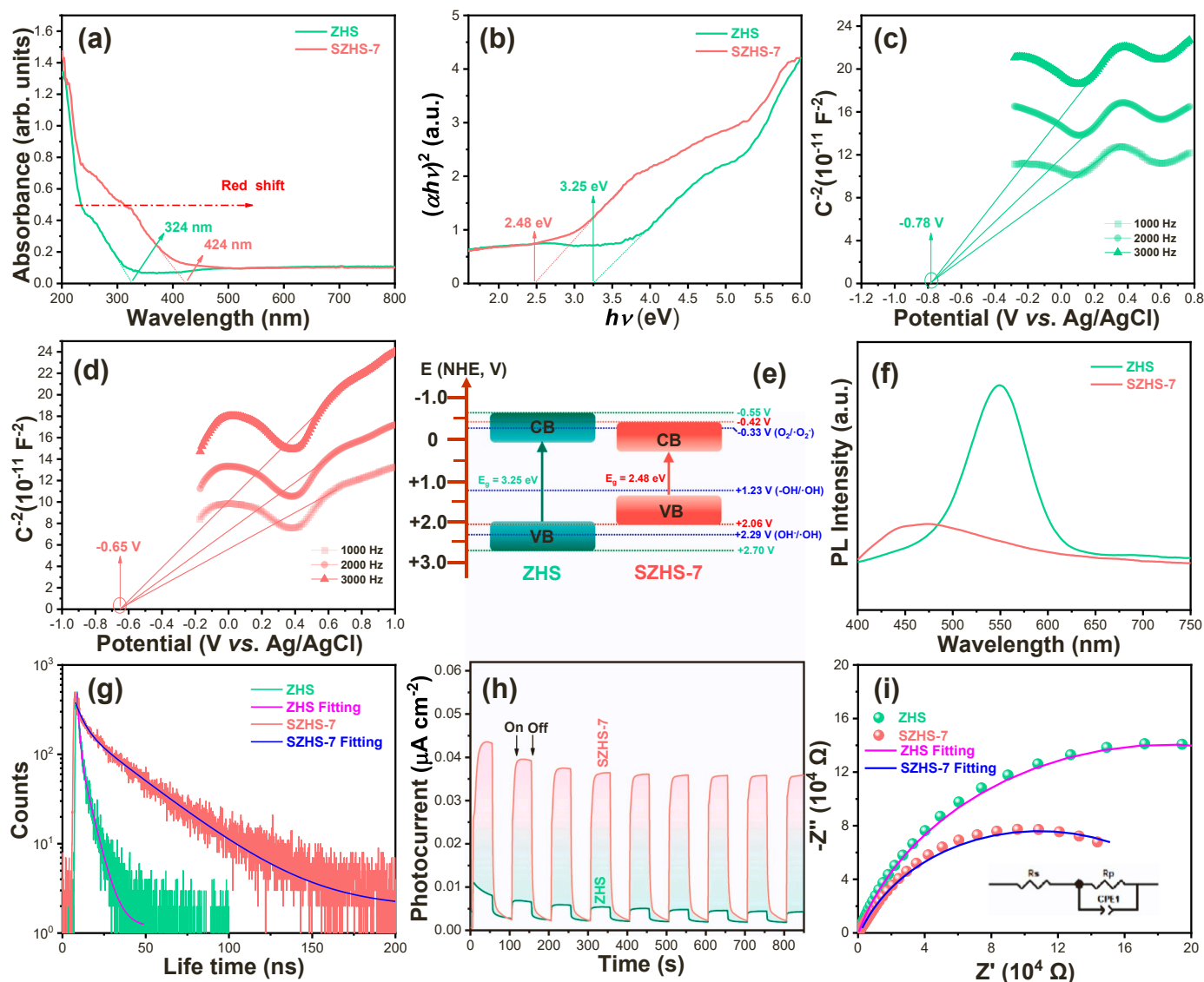
Fig. 3. UV–visible diffuse reflectance spectra (a) and Tauc plots (b) of ZHS and SZHS-7. Mott-Schottky curves of ZHS (c) and SZHS-7 (d), and energy band structure (e) of ZHS and SZHS-7 samples. Room temperature PL spectra (f), the nanosecond time-resolved photoluminescence spectra (g), photocurrent (h) and EIS (i) of ZHS and SZHS-7 (The inset in 3i shows the Randle circuit model).

respectively. Based on the formula ($E_{VB} = E_g - E_{VB}$), the VB position of ZHS and SZHS-7 is determined to be + 2.70 V and + 2.06 V, respectively, the corresponding band structures of ZHS and SZHS-7 were provided (Fig. 3e). As compared with ZHS, the S^{2-} doping changes the band positions and narrows the band gap of ZHS distinctly, which would be a favor for light absorption.

To further understand the function of dual anion defects during the photocatalytic process, the separation and transportation behaviors of photoinduced charges were examined. As shown in Fig. 3f, SZHS-7 exhibits a much lower PL intensity than that of pristine ZHS, suggesting the smallest photogenerated charge recombination behavior [55,56], which stems from the positive contribution of S^{2-} and OVs to significantly enhance the charge separation of photoexcited charge carriers in the system of SZHS-7. To quantificationally clarify the suppressed charge recombination, charge lifetime was performed by time-resolved fluorescence spectra (TRPL), as shown in Fig. 3g and Table 1. The average lifetime increases from 3.72 ns (ZHS) to 26.91 ns (SZHS-7), and the longer fluorescence lifetime implies a more efficient electron-hole pairs separation in SZHS-7. According to the calculated equations (Eqs. (1) and (2)) of electron transfer rate (k_{ET}) and efficiency (η_{ET}), for SZHS-7,

Table 1
The kinetics of emission decay parameters of ZHS and SZHS-7.

Sample	Parameter	Lifetime [ns]	B	Ave. lifetime [ns]	$k_{ET}/$ 10^{10}[s^{-1}]	η_{ET} [%]
ZHS	τ_1	1.07	380.97	3.72	-	-
	τ_2	5.39	120.44			
SZHS-7	τ_1	4.74	186.19	26.91	2.32	86.18
	τ_2	30.19	197.90			

the k_{ET} and η_{ET} are respectively 2.32×10^{10} s^{-1} and 86.18 % (Table 1).

$$k_{ET} = \frac{1}{\tau_{ave(ZHS)}} - \frac{1}{\tau_{ave(SZHS-7)}} \qquad (1)$$

$$\eta_{ET} = 1 - \frac{\tau_{(ZHS)}}{\tau_{(SZHS-7)}} \qquad (2)$$

These results clearly show that the appropriate introduction of S^{2-} and the presence of OVs can effectively promote charge transfer efficiency and inhibit the recombination of photogenerated electrons and

holes [57]. The improved charge transport of SZHS-7 can also be confirmed by the photocurrent density-time (i–t) curves and electrochemical impedance spectroscopy (EIS). From transient photocurrent densities in Fig. 3h, SZHS-7 shows higher photocurrent than that of bare ZHS. The photocurrent intensity of SZHS-7 is about 9.5 times higher than that of pure ZHS, which further proves that the dual anion defects can promote the electron-hole pairs separation action of SZHS-7 [58, 59]. Moreover, EIS spectra in Fig. 3i exhibit that the decreased hemicycle radius of SZHS-7 reflects the lower electric resistance, which is beneficial for charge transport and separation [60]. This result is in line with the above PL and TRPL results. Importantly, the coexistence of S^{2-} doping and OVs could influence the localized electron distribution in SZHS-7 (Fig. S9a and S9b). The enhanced charge density means more localized electrons, which can be derived from the interaction between OVs and adjacent Sn metal atom sites. Whilst the strong interaction between S and Sn atoms can provide a stable and efficient channel for

electron transport (Fig. S10).

3.4. Adsorption and activation of H_2O and O_2 molecules

In principle, during the efficient photocatalytic C_7H_8 oxidation process, the ability of photocatalysts to produce reactive oxygen species (ROSs) is the rate-limiting step [61]. Therefore, the DMPO spin-trapping EPR measurements were supplied to examine the formation of ROSs. As illustrated in Figs. 4a-4c, both ZHS and SZHS-7 can generate·O_2^-,·OH and H_2O_2 radicals, whereas the radicals signal intensities of SZHS-7 are much higher than that of ZHS. This can be attributed to the fact that the band gap of SZHS-7 decreases from 3.25 to 2.48 eV, which makes it easier for electrons excite from the VB to the CB to react with H_2O and O_2 to yield more·OH and·O_2^- (Figs. 4a and 4b) [11,62]. This trend of free radical formation is following the production of H_2O_2, because the efficient carrier separation and migration of the SZHS-7 provide enough
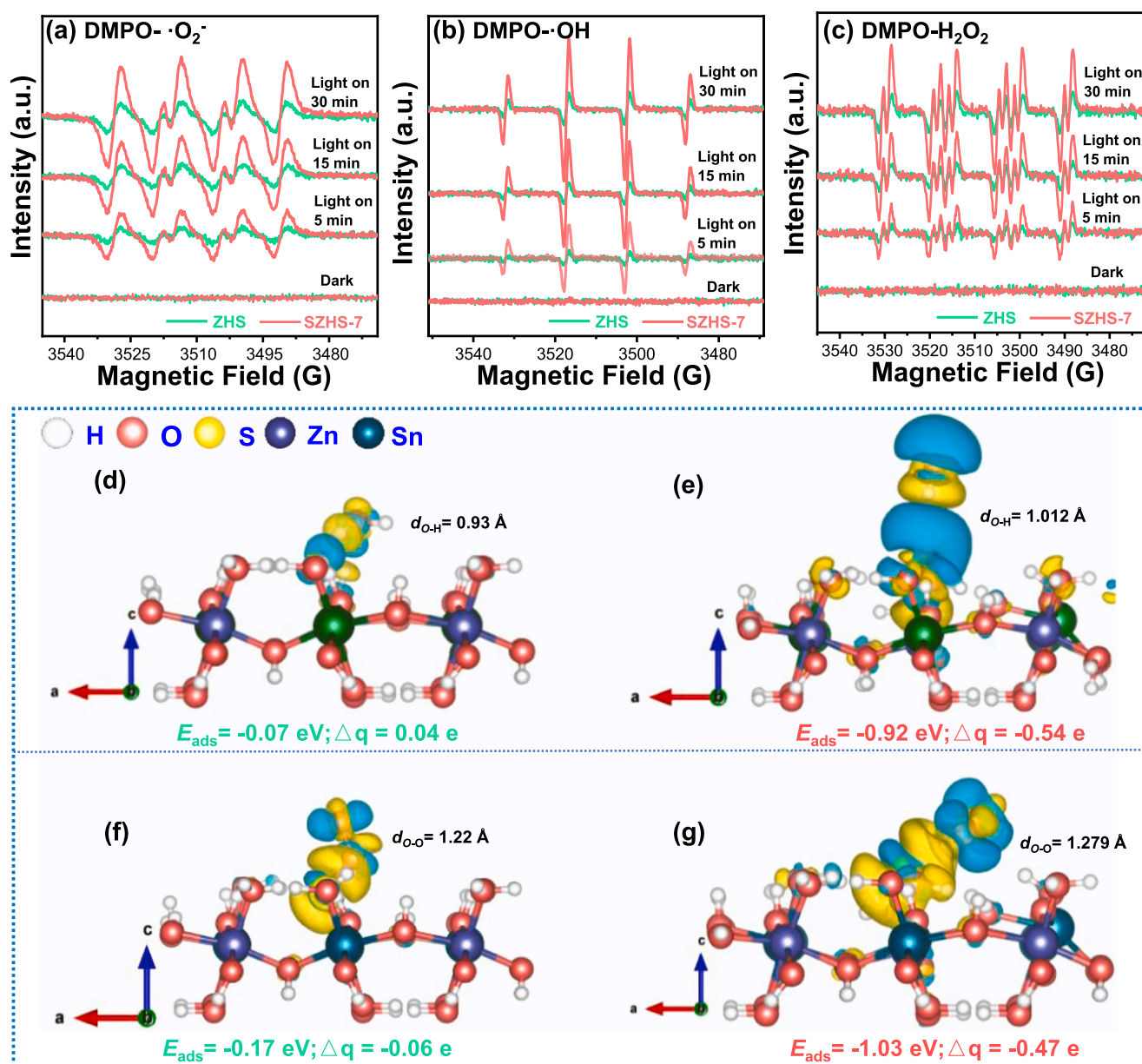

Fig. 4. DMPO spin-trapping EPR spectra for·O_2^- (a),·OH (b) and H_2O_2 (c). Charge density difference calculations for adsorbed H_2O (d, e) and O_2 (f, g) on the surface of ZHS and SZHS-7. E_{ads} and Δq indicate the adsorption energy and the total charge of O_2 (H_2O) molecules on the photocatalyst surface, respectively. All the bond length units are Å (Note: green, gray, yellow, pink and white are Sn, Zn, S, O and H atoms, respectively; cyan shows electron accumulation and yellow denotes electron consumption).

electrons to oxidize H_2O to H_2O_2 (E_φ(H_2O/H_2O_2) = 1.76 V versus. NHE.) [63]. Simultaneously, under the action of photogenerated electrons and holes, H_2O_2 forms·OH (H_2O_2 +e⁻→·OH+OH⁻) and ·O_2^- (H_2O_2 +h⁺→·O_2^-+2 H⁺) respectively, thus increasing the effective generation of ROSs. (Fig. 4c) [64]. The presence of S^{2-} doping and OVs, indeed, work as bifunctional active sites to greatly promote the adsorption and activation of O_2 and H_2O molecules. Whilst the separation of photogenerated carriers was accelerated to contribute to the generation of ROSs, thus giving decently deep oxidation performance of C_7H_8.

In order to better understand the relationship between the electron-transfer pathway of the H_2O/O_2 and the formation of ROSs, DFT was performed on the ZHS and SZHS-7 (200) surfaces. As shown in Fig. 4d-g, the adsorption energies (E_{ads}), charge exchange capacity (Δq) and bond lengths of O_2 and H_2O molecules on ZHS and SZHS-7 were analyzed. The E_{ads} and Δq of H_2O are − 0.07 eV and 0.04 e for ZHS, and − 0.92 eV and − 0.54 e for SZHS-7. This demonstrates that the adsorbed H_2O on the surface with co-generation of S^{2-} doping and OVs would exchange more electrons for the enhanced activation to produce·OH radicals (Fig. 4d and e). Meantime, the E_{ads} of O_2 on the surface of ZHS (E_{ads}=−0.17 eV) is much higher than that of ZHS (E_{ads}=−1.03 eV), and the Δq increases from − 0.06 e for ZHS to − 0.47 e for SZHS-7(Fig. 4f and g). This voices that O_2 molecules are easier to adsorb and activation on the surface of SZHS-7. Significantly, the bond lengths of all molecules adsorbed on the surfaces of SZHS-7 are generally longer than ZHS. Thus, we can further confirm that the construction of dual anion defects to function as active sites not only promote light utilization but also the activation of small molecules on SZHS-7, which is in accord with the increased EPR signals.

3.5. Proposed mechanism of photocatalytic C_7H_8 oxidation

In order to better understand the relationship between dual anion defects and deep oxidation of C_7H_8 on SZHS-7, detailed reaction intermediates and transformation pathways were investigated by combining in situ DRIFTS with theoretical calculations. The attribution of IR peaks during C_7H_8 adsorption and oxidation processes was itemized in Table 2. Fig. 5a shows signal peaks of each substance on ZHS under dark conditions, including benzyl alcohol (1236 and 3568 cm⁻¹) [65,66], benzaldehyde (1413 and 2916 cm⁻¹) [62,67], and benzoic acid (1598 cm⁻¹) [66]. These peaks are intensified during the adsorption process, which can be attributed to the spontaneous exothermic procedure on ZHS surface [67] as revealed by the DFT simulation (E_{ads}=−0.56 eV) (Fig. 6a). Likewise, the peaks of benzyl alcohol (3459 cm⁻¹) [65], benzaldehyde (1280 cm⁻¹) [68] and benzoic acid (1598 cm⁻¹) [66] can be observed on the surface of SZHS-7 (Fig. 5b). However, it is worth noting that the C-H stretching vibration of the aromatic ring (3078 cm⁻¹) [69] and C_7H_8 (2832 cm⁻¹) [70] can be only observed on the surface of SZHS-7. This phenomenon can be attributed

to the introduction of dual anion defects enhancing the adsorption of C_7H_8 molecules (E_{ads}=−1.75 eV) (Fig. 6b). Meanwhile, the adsorption site of C_7H_8 changes from the O site to the S one (Fig. 6c and d), which is conducive to the activation of C_7H_8. Hence, SZHS-7 with dual anion defects can greatly enhance the charge transfer (Δq from −0.39 to −1.07 e) between adsorbed molecules (C_7H_8, H_2O and O_2) to facilitate the adsorption and chemical activation of C_7H_8, which is considered as the premise of excellent photocatalytic performance.

After the adsorption equilibrium is achieved, the time-dependent IR spectra on ZHS and SZHS-7 were monitored dynamically under UV light irradiation. As for ZHS (Fig. 6c), the symmetric C-H stretching vibration of CH_2 group bands of benzyl species at 2921 cm⁻¹ [71] is weak, indicating that the benzene ring can't be effectively activated on ZHS under light irradiation. Some aromatic rings containing intermediates (e.g., the benzyl alcohol (1056, 1278 and 3459 cm⁻¹) [67,69,72] and benzoic acid (1400 and 1598 cm⁻¹) [66,73] are also observed. It is worth noting that the benzyl alcohol on ZHS is continuously accumulated, resulting in a low mineralization rate. As for SZHS-7 (Fig. 6d), the bands at 2856 cm⁻¹ [71] and 3042 cm⁻¹ [62] represent symmetric C-H stretching vibration of CH_2 group bands of benzyl species and the C-H stretching vibrations of aromatic rings, respectively. The two peak intensities decrease gradually with the extension of radiation, indicative of C_7H_8 is activated to be deeply oxidized. Consequently, the oxidizing species can be detected and recognized as benzyl alcohol (1278 and 3459 cm⁻¹) [67,69], benzaldehyde (1445 and 1620 cm⁻¹) [65,66] and benzoic acid (1391 and 1598 cm⁻¹) [65,66]. Notably, the intensities of benzaldehyde and benzoic acid (1391 cm⁻¹) locate at 1445, 1620 and 1391 cm⁻¹ [65,66] are amplified on SZHS-7. It is well known that benzaldehyde can be further oxidized to benzoic acid, to which is a key intermediate in the deep oxidation process of C_7H_8 [74]. In addition, in order to further confirm that SZHS-7 with dual anion defects has strong deep oxidation capacity, in situ DRIFTS were provided to dynamically record the variation of NO on the photocatalyst's surface (Fig. S11 and Table S3). The absorption bands (1598, 1394, 1219, 940 and 1726 cm⁻¹) [75–78] belonging to the NO_2(N_2O_4) can be observed on the surface of the two samples. This fact confirms that the two samples can be able to adsorb NO molecular. With regard to the photocatalytic degradation process on SZHS-7 (Fig. S11d), the NO_2 is consumed, the NO_3^- (1004 cm⁻¹) [79] and NO_2^- (1292 and 886 cm⁻¹) [77,80] is accumulated apparently. In addition, a new absorption peak of NO⁻ (1162 cm⁻¹) can be also found during the reaction [80]. Under the action of O_2 and ROSs, the reaction was further formed into NO_3^- (NO⁻+O_2→NO_2^-+·O_2^-→NO_3^-) [79], which realizes the deep oxidation of NO and avoids the formation of the toxic byproduct NO_2.

Based on the solid experiment and DFT results, we revealed in depth the key role of OVs and S^{2-} doping in the reaction of photocatalytic C_7H_8 oxidation. The possible photocatalysis mechanism of SZHS-7 is shown in

Table 2
The main intermediate products of photocatalytic oxidation of C_7H_8 as determined by *in-situ* DRIFTS measurements.

|	ZHS			SZHS-7		
	Wavenumber (cm⁻¹)	Assignment	Ref.	Wavenumber (cm⁻¹)	Assignment	Ref.
Adsorption mode	1236	benzyl alcohol	[66]	1280	benzaldehyde	[68]
	1413	benzaldehyde	[67]	1598	benzoic acid	[66]
	1598	benzoic acid	[66]	2832	toluene	[70]
	2916	benzaldehyde	[62]	3078	C-H stretching vibration of aromatic ring	[69]
	3568	benzyl alcohol	[65]	3459	benzyl alcohol	[65]
Reaction mode	1056	benzyl alcohol	[72]	1278	benzyl alcohol	[69]
	1278	benzyl alcohol	[69]	1391	benzoic acid	[65]
	1400	benzoic acid	[73]	1445	benzaldehyde	[66]
	1598	benzoic acid	[66]	1598	benzoic acid	[66]
	2921	the symmetric C-H stretching vibration of CH_2 group	[71]	1620	benzaldehyde	[65]
	3459	benzyl alcohol	[67]	2856	C-H stretching vibration of CH_2 group bands of benzyl species	[71]
	3576	benzyl alcohol	[65]	3042	C-H stretching vibrations of aromatic rings	[62]
				3459	benzyl alcohol	[67]
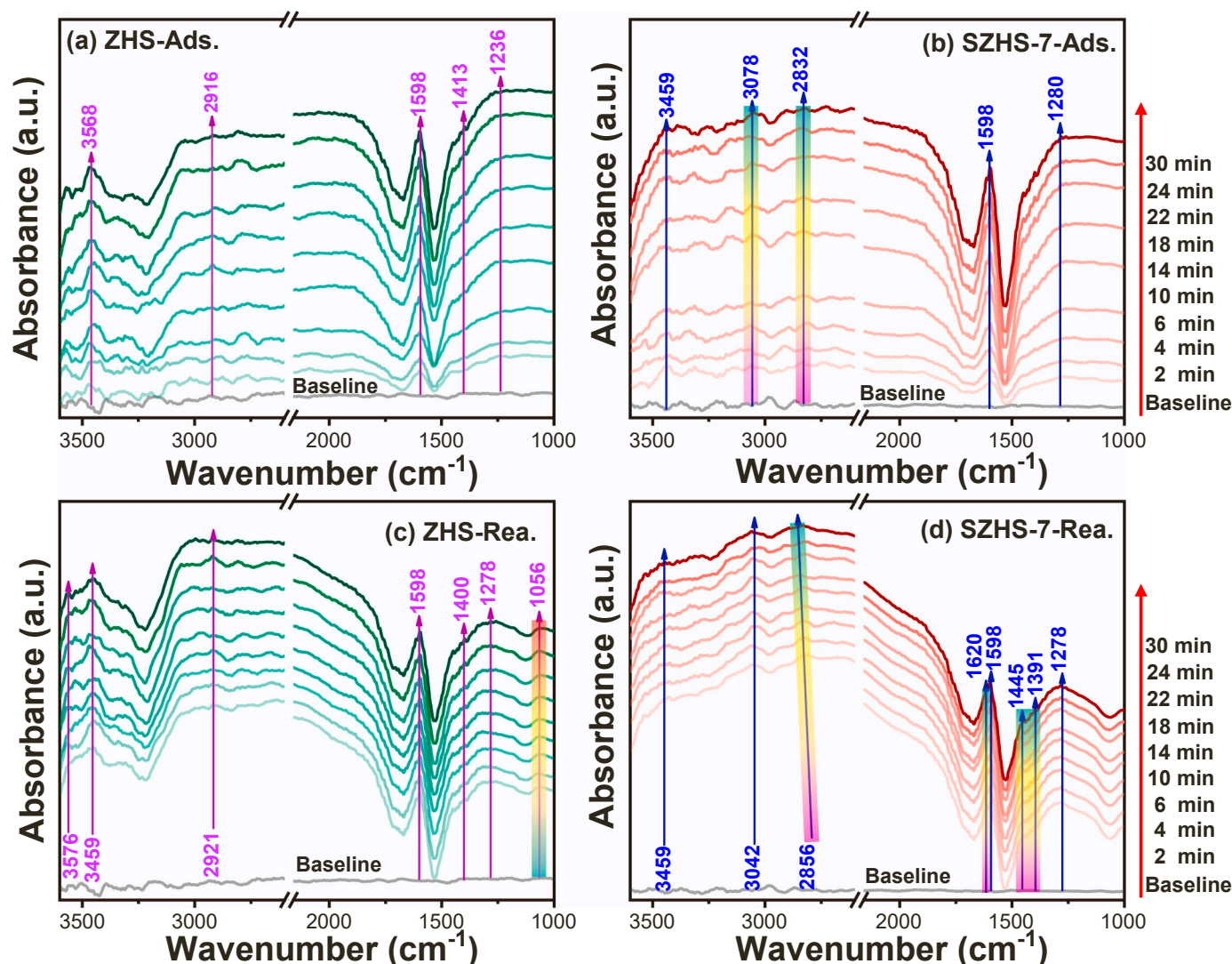
Fig. 5. *In situ* FT-IR spectra of C_7H_8 adsorption (a and b) and photocatalytic reaction (c and d) processes over ZHS and SZHS-7.

Fig. 6e. 1) As compared with ZHS, the S^{2-} doping introduced more accessible OVs with low formation energy, and the OVs can localize rich electrons to activate the adsorption of small molecules and C_7H_8. 2) The substitution of O^{2-} by the S^{2-} could induce abundant surface OVs electron traps to promote the activation of lattice oxygen, improve the redox performance, and facilitate the oxidation purification of C_7H_8. 3) The synergistic action of the dual anion defects provides sufficient localized electrons for the formation of $\cdot O_2^-$ and H_2O_2, and the separated photo-generated holes for the formation of $\cdot OH$. Thereby, the band gap of ZHS is narrowed by the appropriate amount of S substitution and the introduction of OVs, which extends the light absorption capacity. Meanwhile, OVs synergy with nearby active S sites to ameliorate localized electron distribution and form a rapid charge transfer channel, promoting carrier separation and migration. All of these render SZHS-7 to perform a highly effective photocatalytic C_7H_8 and NO removal performance.

4. Conclusions

In summary, we have designed and fabricated, for the first time, ZHS with dual anion defects (S^{2-} and OVs) by a simple water-bath microwave method. According to XRD, XPS and EPR results, the presence of S element and OVs in SZHS-7 was determined. The photocatalysts exhibited excellent NO (49.8 %) and C_7H_8 removal rates (92.5 %). A combination of photoelectrochemical measurements with DFT simulations revealed that S^{2-} doping offers a charge transport channel in the interstice sites of the lattice. The results of the EPR free radical capture experiment and in situ DRIFTS also confirmed that the coexistence of S^{2-} doping and OVs can provide enough adsorption sites for small molecules to react on the photocatalyst surface, thus promoting the formation of active free radicals and achieve the deep oxidation of C_7H_8 and NO. Hence, this study demonstrates the feasibility of constructing bi-anionic active sites modified photocatalysts by introducing OVs in semiconductor photocatalysts with nonmetallic ion doping, thus providing a feasible strategy for the development of efficient environmental remediation photocatalysts.

CRediT authorship contribution statement

Bangfu Chen: Investigation, Writing – original draft, Methodology, Formal analysis. **Zeyong Meng:** Data curation, Formal analysis. **Ping Ouyang:** Conceptualization, Supervision, Project administration. **Youyu Duan** and **Yuhan Li:** Investigation, Formal analysis, Conceptualization, Methodology, Writing – review & editing, Resources, Supervision. **Wanjun Wang** and **Fan Dong:** Resources, Project administration.
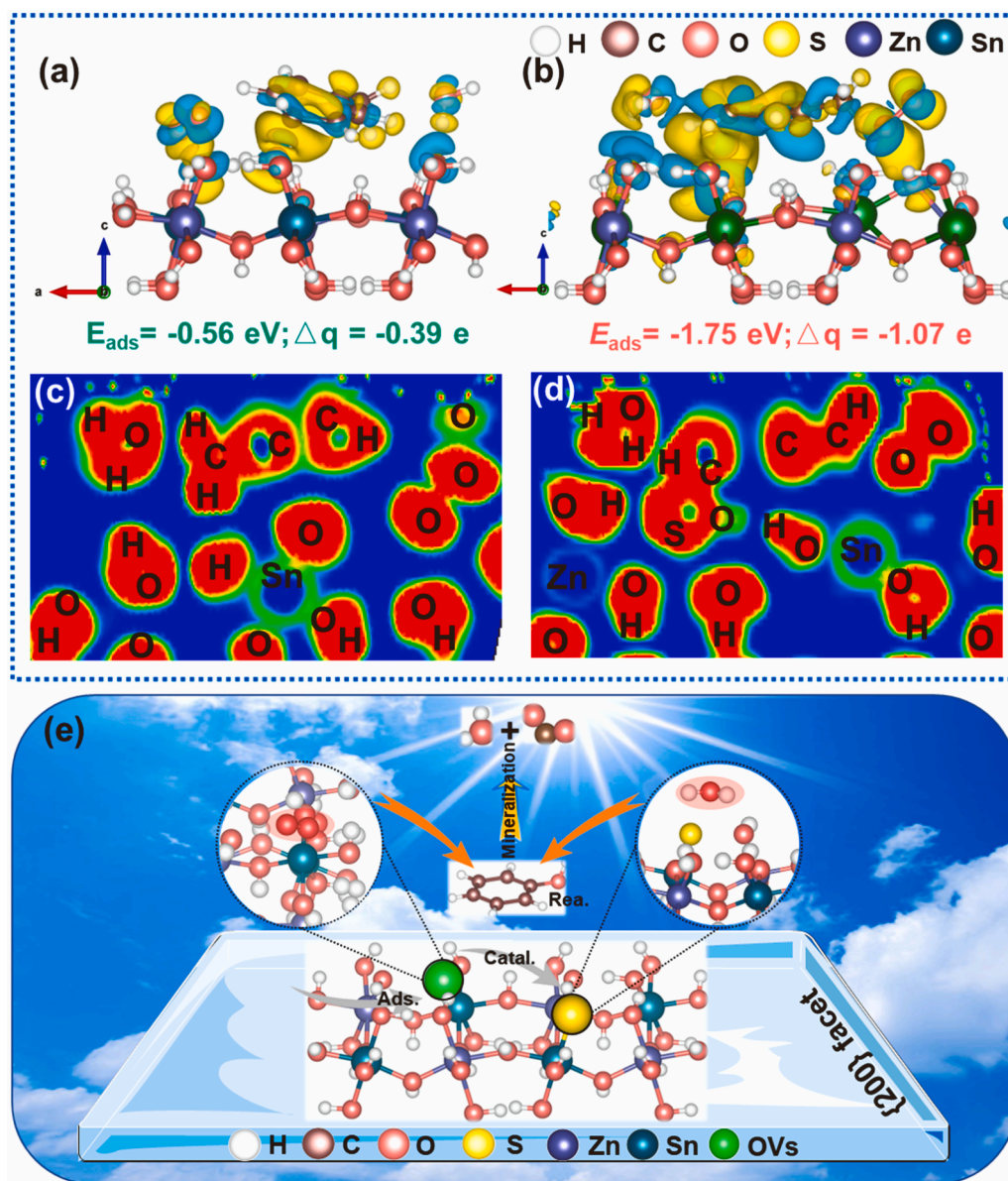
Fig. 6. Charge difference (Δq) and electron local function (ELF) of ZHS (a, c) and SZHS-7 (b, d): optimized $O_2/H_2O/C_7H_8$ adsorption with side views (the color definition is the same as the Fig. 4 and copper is C atoms), E_{ads} and Δq indicated the adsorption energy and the total charge of $O_2/H_2O/C_7H_8$ molecules on the photocatalyst surface, respectively; Schematic illustration of proposed mechanisms for C_7H_8 oxidation over the SZHS-7 photocatalyst (e).

Declaration of Competing Interest

The authors declare that they have no known competing financial interests or personal relationships that could have appeared to influence the work reported in this paper.

Data availability

Data will be made available on request.

Acknowledgements

Appendix A. Supporting information

Supplementary data associated with this article can be found in the online version at doi:10.1016/j.apcatb.2023.123093.

References

[1] Y. Gao, H. Wang, X. Zhang, S. Jing, Y. Peng, L. Qiao, M. Zhou, D. Huang, Q. Wang, X. Li, L. Li, J. Feng, Y. Ma, Y. Li, Estimating secondary organic aerosol production from toluene photochemistry in a megacity of China, Environ. Sci. Technol. 53 (2019) 8664–8671, https://doi.org/10.1021/acs.est.9b00651.

[2] X. Cao, Z. Chen, R. Lin, W. Cheong, S. Liu, J. Zhang, Q. Peng, C. Chen, T. Han, X. Tong, Y. Wang, R. Shen, W. Zhu, D. Wang, Y. Li, A photochromic composite with

enhanced carrier separation for the photocatalytic activation of benzylic C-H bonds in toluene, Nat. Catal. 1 (2018) 704–710, https://doi.org/10.1038/s41929-018-0128-z.

[3] F. Li, D. Tian, Y. Fan, R. Lee, G. Lu, Y. Yin, B. Qiao, X. Zhao, Z. Xiao, Z. Jiang, Chiral acid-catalysed enantioselective C−H functionalization of toluene and its derivatives driven by visible light, Nat. Commun. 10 (2019) 1774, https://doi.org/10.1038/s41467-019-09857-9.

[4] H. Duan, J. Liu, M. Xu, Y. Zhao, X. Ma, J. Dong, X. Zheng, J. Zheng, C. Allen, M. Danaie, Y. Peng, T. Issariyakul, D. Chen, A. Kirkland, J. Buffet, J. Li, S. Tsang, D. Hare, Molecular nitrogen promotes catalytic hydrodeoxygenation, Nat. Catal. 2 (2019) 1078–1087, https://doi.org/10.1038/s41929-019-0368-6.

[5] X. Wei, K. Li, X. Zhang, Q. Tong, J. Ji, Y. Cai, B. Gao, W. Zou, L. Dong, CeO_2 nanosheets with anion-induced oxygen vacancies for promoting photocatalytic toluene mineralization: Toluene adsorption and reactive oxygen species, Appl. Catal. B Environ. 317 (2022), 121694, https://doi.org/10.1016/j.apcatb.2022.121694.

[6] Y. Zhang, J. Zhao, H. Wang, B. Xiao, W. Zhang, X. Zhao, T. Lv, M. Thangamuthu, J. Zhang, Y. Guo, J. Ma, L. Lin, J. Tang, R. Huang, Q. Liu, Single-atom Cu anchored catalysts for photocatalytic renewable H_2 production with a quantum efficiency of 56%, Nat. Commun. 58 (2022) 13, https://doi.org/10.1038/s41467-021-27698-3.

[7] X. Qiu, Y. Sang, H. Wu, X. Xue, Z. Yan, Y. Wang, Z. Cheng, X. Wang, H. Tan, S. Song, G. Zhang, X. Zhang, K. Houk, N. Jiao, Cleaving arene rings for acyclic alkenylnitrile synthesis, Nature 597 (2021) 64–69, https://doi.org/10.1038/s41586-021-03801-y.

[8] Y. Guo, J. Chen, Y. Zhao, Y. Lou, In-situ anchoring Pb-Free $Cs_3Bi_2Br_9$@BiOBr quantum dots on NH_x-Rich silica with enhanced blue emission and satisfactory stability for photocatalytic toluene oxidation, ChemSusChem 15 (2022), e202200793, https://doi.org/10.1002/cssc.202200793.

[9] Z. Bai, X. Tan, L. Chen, B. Hu, Y. Tan, Y. Mao, S. Shen, J. Gu, C. Au, Z. Liang, S. Yin, Efficient photocatalytic toluene selective oxidation over $Cs_3Bi_{1.8}Sb_{0.2}Br_9$ nanosheets: enhanced charge carriers generation and C–H bond dissociation, Chem. Eng. J. 247 (2022), 116983 https://doi-org-ssl.3436.top/10.1016/j.ces.2021.116983.

[10] Y. Zhang, M. Wu, Y. Wang, Y. Kwok, W. Pan, W. Szeto, H. Huang, D. Leung, Fluorinated TiO_2 coupling with α-MnO_2 nanowires supported on different substrates for photocatalytic VOCs abatement under vacuum ultraviolet irradiation, Appl. Catal. B Environ. 280 (2021), 119388, https://doi.org/10.1016/j.apcatb.2020.119388.

[11] Z. Rao, G. Lu, L. Chen, A. Mahmood, G. Shi, Z. Tang, X. Xie, J. Sun, Photocatalytic oxidation mechanism of gas-phase VOCs: unveiling the role of holes, •OH and •O_2^-, Chem. Eng. J. 430 (2022), 132766 https://doi.org/10.1016/j.cej.2021.132766.

[12] M. Malayeri, C. Lee, J. Niu, J. Zhu, F. Haghighat, Kinetic modeling and reaction mechanism of toluene and by-products in photocatalytic oxidation reactor, Chem. Eng. J. 427 (2022), 131536, https://doi.org/10.1016/j.cej.2021.131536.

[13] C. Liang, C. Li, Y. Zhu, X. Du, Y. Zeng, Y. Zhou, J. Zhao, S. Li, X. Liu, Q. Yu, Y. Zhai, Light-driven photothermal catalysis for degradation of toluene on CuO/TiO_2 Composite: dominating photocatalysis and auxiliary thermalcatalysis, Appl. Surf. Sci. 601 (2022), 154144, https://doi.org/10.1016/j.apsusc.2022.154144.

[14] X. Fu, J. Wang, D. Huang, S. Meng, Z. Zhang, L. Li, T. Miao, S. Chen, Trace amount of SnO_2-Decorated $ZnSn(OH)_6$ as highly efficient photocatalyst for decomposition of gaseous benzene: synthesis, photocatalytic activity, and the unrevealed synergistic effect between $ZnSn(OH)_6$ and SnO_2, ACS Catal. 6 (2016) 957–968, https://doi.org/10.1021/acscatal.5b02593.

[15] X. Fu, D. Huang, Y. Qin, L. Li, X. Jiang, S. Chen, Effects of preparation method on the microstructure and photocatalytic performance of $ZnSn(OH)_6$, Appl. Catal. B Environ. 148 (2014) 532–542, https://doi.org/10.1016/j.apcatb.2013.11.039.

[16] H. Wang, X. Yuan, Y. Wu, G. Zeng, W. Tu, C. Sheng, Y. Deng, F. Chen, J. Chew, Plasmonic Bi nanoparticles and BiOCl sheets as cocatalyst deposited on perovskite-type $ZnSn(OH)_6$ microparticle with facet-oriented polyhedron for improved visible-light-driven photocatalysis, Appl. Catal. B Environ. 209 (2017) 543–553, https://doi.org/10.1016/j.apcatb.2017.03.024.

[17] H. Yu, R. Lai, H. Zhuang, Z. Zhang, X. Wang, Controllable synthesis of crystallographic facet-oriented polyhedral $ZnSn(OH)_6$ microcrystals with assistance of a simple ion, CrystEngComm 14 (2012) 8530–8535, https://doi.org/10.1039/C2CE25872B.

[18] X. Fu, D. Leung, X. Wang, W. Xue, X. Fu, Photocatalytic reforming of ethanol to H_2 and CH_4 over $ZnSn(OH)_6$ nanocubes, Int. J. Hydrog. Energy 36 (2011) 1524–1530, https://doi.org/10.1016/j.ijhydene.2010.10.090.

[19] C. Zhang, D. He, S. Fu, G. Zeng, Q. Liang, Y. Yang, D. Huang, W. Wang, Y. Zhou, Silver iodide decorated $ZnSn(OH)_6$ hollow cube: room-temperature preparation and application for highly efficient photocatalytic oxytetracycline degradation, Chem. Eng. J. 421 (2021), 129810, https://doi.org/10.1016/j.cej.2021.129810.

[20] M. Pham, D. Bui, I. Lin, N. Phuong, Y. Huang, J. Cao, S. You, Y. Wang, Enhanced near-visible-light photocatalytic removal of formaldehyde over Au-assisted ZnSn $(OH)_6$ microcubes, Environ. Technol. Innov. 20 (2020), 101112, https://doi.org/10.1016/j.eti.2020.101112.

[21] Y. Zhang, L. Wang, M. Yang, J. Wang, J. Shi, Carbon quantum dots sensitized ZnSn $(OH)_6$ for visible light-driven photocatalytic water purification, Appl. Surf. Sci. 466 (2019) 515–524, https://doi.org/10.1016/j.apsusc.2018.10.087.

[22] Q. Chen, S. Ma, H. Jiao, B. Wang, G. Zhang, D. Gengzang, L. Liu, H. Yang, Sodium alginate assisted hydrothermal method to prepare praseodymium and cerium co-doped $ZnSn(OH)_6$ hollow microspheres and synergistically enhanced ethanol sensing performance, Sens. Actuators B Chem. 252 (2017) 295–305, https://doi.org/10.1016/j.snb.2017.06.015.

[23] N. Gomari, I. Kazeminezhad, S. Ghahfarokhi, Impact of morphology evolution of $ZnSn(OH)_6$ microcubes on photocatalytic activity of $ZnSn(OH)_6/SnO_2/rGO$ ternary

[24] nanocomposites for efficient degradation of organic pollutants, Opt. Mater. 113 (2021), 110878, https://doi.org/10.1016/j.optmat.2021.110878.

[24] Q. Xu, L. Zhang, B. Cheng, J. Fan, J. Yu, S-scheme heterojunction photocatalyst, Chem 6 (2020) 1543–1559, https://doi.org/10.1016/j.chempr.2020.06.010.

[25] D. Ma, L. Yang, Z. Sheng, Y. Chen, Photocatalytic degradation mechanism of benzene over $ZnWO_4$: revealing the synergistic effects of Na-doping and oxygen vacancies, Chem. Eng. J. 405 (2021), 126538, https://doi.org/10.1016/j.cej.2020.126538.

[26] F. Yu, Q. Deng, H. Li, Y. Xia, W. Hou, A general strategy to synthesize single-atom metal-oxygen doped polymeric carbon nitride with highly enhanced photocatalytic water splitting activity, Appl. Catal. B Environ. 323 (2023), 122180, https://doi.org/10.1016/j.apcatb.2022.122180.

[27] S. Yang, X. Li, G. Zeng, M. Cheng, D. Huang, Y. Liu, Zhou Zhou, W. Xiong, Y. Yang, W. Wang, G. Zhang, Materials institute lavoisier (MIL) based materials for photocatalytic applications, Coord. Chem. Rev 438 (2021), 213874, https://doi.org/10.1016/j.ccr.2021.213874.

[28] S. Wang, X. Ding, N. Yang, G. Zhan, X. Zhang, G. Dong, L. Zhang, H. Chen, Insight into the effect of bromine on facet-dependent surface oxygen vacancies construction and stabilization of Bi_2MoO_6 for efficient photocatalytic NO removal, Appl. Catal. B Environ. 265 (2020), 118585, https://doi.org/10.1016/j.apcatb.2019.118585.

[29] J. Nie, Q. Hassan, Y. Jia, J. Gao, J. Peng, J. Lu, F. Zhang, G. Zhu, Q. Wang, La-doped $ZnWO_4$ nanorods with enhanced photocatalytic activity for NO removal: effects of La doping and oxygen vacancies, Inorg. Chem. Front. 7 (2020) 356–368, https://doi.org/10.1039/C9QI01152H.

[30] M. Chen, S. Wei, J. Wu, J. Li, B. Fu, X. Zhu, Sulfur doped Bi-MOF with adjustable band gap for tetracycline removal under visible light, Colloids Surf. A Physicochem. Eng. Asp. 664 (2023), 131186, https://doi.org/10.1016/j.colsurfa.2023.131186.

[31] Y. Song, B. Yang, Z. Ma, Y. Song, J. Sun, Fabrication of $S_x/In_2O_{3−x}$ based microsphere for photoexcitation enhancing the NO_2 gas detection properties, Sens. Actuators B Chem. 379 (2023), 133162, https://doi.org/10.1016/j.snb.2022.133162.

[32] A. Abdeta, Q. Wu, D. Kuo, P. Li, H. Zhang, T. Huang, J. Zhang, M. Mosisa, J. Lin, X. Chen, Mo(S,O)/(Ce,Mo)(S,O) sulfo-oxide with heterovalent metal states for efficient visible-light-driven hydrogen evolution and pollutant reduction via in-situ generated protons, Int. J. Hydrog. Energy 48 (2023) 10841–10858, https://doi.org/10.1016/j.ijhydene.2022.12.155.

[33] Y. Guo, S. Li, F. Yang, C. Li, Y. Guo, K. Xuan, G. Wang, Y. Liu, J. Li, Efficient charge separation in sulfur doped $AgFeO_2$ photocatalyst for enhanced photocatalytic U(VI) reduction: the role of doping and mechanism insights, J. Hazard. Mater. 440 (2022), 129734, https://doi.org/10.1016/j.jhazmat.2022.129734.

[34] Q. Liu, Z. Liu, D. Liu, W. Wang, Z. Zhao, F. Cui, G. Li, Oxygen vacancy-rich ultrathin sulfur-doped bismuth oxybromide nanosheet as a highly efficient visible-light responsive photocatalyst for environmental remediation, Chem. Eng. J. 360 (2019) 838–847, https://doi.org/10.1016/j.cej.2018.12.038.

[35] C. Filippi, D. Singh, C. Umrigar, All-electron local-density and generalized-gradient calculations of the structural properties of semiconductors, Phys. Rev. B 50 (1994) 14947, https://doi.org/10.1103/PhysRevB.50.14947.

[36] Burke Perdew, Ernzerhof, Generalized gradient approximation made simple, Phys. Rev. Lett. 77 (1996) 3865, https://doi.org/10.1103/PhysRevLett.77.3865.

[37] G. Henkelman, B. Uberuaga, H. Jónsson, A climbing image nudged elastic band method for finding saddle points and minimum energy paths, J. Chem. Phys. 113 (2000) 9901–9904, https://doi.org/10.1063/1.1329672.

[38] L. Yan, Q. Wang, W. Qu, T. Yan, H. Li, P. Wang, D. Zhang, Tuning $Ti^{δ+}$-Vo-$Pt^{δ+}$ interfaces over Pt/TiO_2 catalysts for efficient photocatalytic oxidation of toluene, Chem. Eng. J. 431 (2022), 134209, https://doi.org/10.1016/j.cej.2021.134209.

[39] J. Araña, D. Sousa, O. Díaz, E. Melián, J. Rodríguez, Effect of NO_2 and NO_3/HNO_3 adsorption on NO photocatalytic conversion, Appl. Catal. B Environ. 244 (2019) 660–670, https://doi.org/10.1016/j.apcatb.2018.12.005.

[40] H. Wang, Y. Sun, G. Jiang, Y. Zhang, H. Huan, Z. Wu, S.C. Lee, F. Dong, Unraveling the mechanisms of visible light photocatalytic NO purification on earth-abundant insulator-based core–shell heterojunctions, Environ. Sci. Technol. 52 (2018) 1479–1487, https://doi.org/10.1021/acs.est.7b05457.

[41] J. Li, X. Dong, Y. Sun, G. Jiang, Y. Chu, S.C. Lee, F. Dong, Tailoring the rate-determining step in photocatalysis via localized excess electrons for efficient and safe air cleaning, Appl. Catal. B Environ. 239 (2018) 187–195, https://doi.org/10.1016/j.apcatb.2018.08.019.

[42] Y. Li, B. Chen, P. Ouyang, Y. Duan, W. Ong, F. Dong, Engineering $ZnSn(OH)_6$ with ternary active sites-directed hydroxyl vacancies for robust deep C_6H_6 photo-oxidation: experiment and DFT calculations, Chem. Eng. J. 451 (2023), 138695, https://doi.org/10.1016/j.cej.2022.138695.

[43] L. Wang, K. Tang, Z. Liu, D. Wang, J. S, W. Cheng, Single-crystalline $ZnSn(OH)_6$ hollow cubes via self-templated synthesis at room temperature and their photocatalytic properties, J. Mater. Chem. 21 (2011) 4352–4357, https://doi.org/10.1039/C0JM03734F.

[44] X. Hu, H. Zhao, Y. Liang, R. Chen, Energy level mediation of $(BiO)_2CO_3$ via Br doping for efficient molecular oxygen activation and ciprofloxacin photodegradation, Appl. Catal. B Environ. 258 (2019), 117966, https://doi.org/10.1016/j.apcatb.2019.117966.

[45] X. Lian, Z. Chen, X. Yu, T. Fan, Y. Dong, H. Zhai, W. Fang, X. Yi, Enhancing the photocatalytic activity of $ZnSn(OH)_6$ achieved by gradual sulfur doping tactics, Nanoscale 11 (2019) 9444–9456, https://doi.org/10.1039/C9NR01103J.

[46] Y. Zhang, J. Shi, Z. Huang, X. Guan, S. Zong, C. Cheng, B. Zheng, L. Guo, Synchronous construction of CoS_2 in-situ loading and S doping for g-C_3N_4:

enhanced photocatalytic H₂-evolution activity and mechanism insight, Chem. Eng. J. 401 (2020), 126135, https://doi.org/10.1016/j.cej.2020.126135.

[47] L. Han, J. Liu, Z. Wang, K. Zhang, H. Luo, B. Xu, X. Zou, X. Zheng, B. Ye, X. Yu, Shape-controlled synthesis of ZnSn(OH)₆ crystallites and their HCHO-sensing properties, CrystEngComm 14 (2012) 3380–3386, https://doi.org/10.1039/C2CE06583E.

[48] Z. Qin, Y. Huang, Q. Wang, J. Qi, X. Xing, Y. Zhang, Controllable synthesis of well-dispersed and uniform-sized single crystalline zinc hydroxystannate nanocubes, CrystEngComm 12 (2010) 4156–4160, https://doi.org/10.1039/C0CE00152J.

[49] H. Yu, D. Ge, Y. Wang, S. Zhu, X. Wang, M. Huo, Y. Lu, Facile synthesis of Bi-modified Nb-doped oxygen defective BiOCl microflowers with enhanced visible-light-driven photocatalytic performance, J. Alloy. Compd. 786 (2019) 155–162, https://doi.org/10.1016/j.jallcom.2019.01.323.

[50] Y. Lu, X. Jia, Z. Ma, Y. Li, S. Yue, X. Liu, J. Zhang, W⁵⁺–W⁵⁺ pair induced LSPR of W₁₈O₄₉ to sensitize ZnIn₂S₄ for full-spectrum solar-light-driven photocatalytic hydrogen evolution, Adv. Funct. Mater. 32 (2022), 2203638, https://doi.org/10.1002/adfm.202203638.

[51] G. Zhao, J. Ding, F. Zhou, Q. Zhao, K. Wang, X. Zhao, Q. Gao, Insight into a novel microwave-assisted W doped BiVO₄ self-assembled sphere with rich oxygen vacancies oriented on rGO (W-BiVO₄₋ₓ/rGO) photocatalyst for efficient contaminants removal, Sep. Purif. Technol. 277 (2021), 119610, https://doi.org/10.1016/j.seppur.2021.119610.

[52] Y. Li, M. Yuan, H. Yang, K. Shi, Z. Sun, H. Li, C. Nan, Ge. Sun, Quantitative decorating Ni-sites for water-oxidation with the synergy of electronegative sites and high-density spin state, Appl. Catal. B Environ. 323 (2023), 122167, https://doi.org/10.1016/j.apcatb.2022.122167.

[53] T. Gani, H. Kulik, Where does the density localize? convergent behavior for global hybrids, range separation, and DFT+U, J. Chem. Theory Comput. 12 (2016) 5931–5945, https://doi.org/10.1021/acs.jctc.6b00937.

[54] H. Li, Y. Cui, W. Hong, B. Xu, Enhanced photocatalytic activities of BiOI/ZnSn (OH)₆ composites towards the degradation of phenol and photocatalytic H₂ production, Chem. Eng. J. 228 (2013) 1110–1120, https://doi.org/10.1016/j.cej.2013.05.086.

[55] C. Feng, L. Tang, Y. Deng, G. Zeng, J. Wang, Y. Liu, Z. Chen, J. Yu, J. Wang, Enhancing optical absorption and charge transfer: synthesis of S-doped h-BN with tunable band structures for metal-free visible-light-driven photocatalysis, Appl. Catal. B Environ. 256 (2019), 117827, https://doi.org/10.1016/j.apcatb.2019.117827.

[56] W. Cui, J. Li, W. Cen, Y. Sun, S.C. Lee, F. Dong, Steering the interlayer energy barrier and charge flow via bioriented transportation channels in g-C₃N₄: enhanced photocatalysis and reaction mechanism, J. Catal. 352 (2017) 351–360, https://doi.org/10.1016/j.jcat.2017.05.017.

[57] F. Chen, Z. Ma, L. Ye, T. Ma, T. Zhang, Y. Zhang, H. Huang, Macroscopic spontaneous polarization and surface oxygen vacancies collaboratively boosting CO₂ photoreduction on BiOIO₃ single crystals, Adv. Mater. 32 (2020), 1908350, https://doi.org/10.1002/adma.201908350.

[58] T. Li, C. Wang, T. Wang, L. Zhu, Highly efficient photocatalytic degradation toward perfluorooctanoic acid by bromine doped BiOI with high exposure of (001) facet, Appl. Catal. B Environ. 268 (2020), 118442, https://doi.org/10.1016/j.apcatb.2019.118442.

[59] W. Cui, J. Li, F. Dong, Y. Sun, G. Jiang, W. Cen, S.C. Lee, Z. Wu, Highly efficient performance and conversion pathway of photocatalytic NO oxidation on SrO-clusters@amorphous carbon nitride, Environ. Sci. Technol. 51 (2017) 10682–10690, https://doi.org/10.1021/acs.est.7b00974.

[60] Z. He, B. Chen, Y. Li, P. Ouyang, Y. Duan, F. Dong, Deep NO oxidation in Zn₂SnO₄ by dual-anionic-defects engineering, Sep. Purif. Technol. 18 (2023), 123886, https://doi.org/10.1016/j.seppur.2023.123886.

[61] J. Li, X. Dong, G. Zhang, W. Cui, W. Cen, Z. Wu, S. Lee, F. Dong, Probing ring-opening pathways for efficient photocatalytic toluene decomposition, J. Mater. Chem. A 7 (2019) 3366–3374, https://doi.org/10.1039/C8TA11627J.

[62] X. Zhang, K. Yue, R. Rao, J. Chen, Q. Liu, Y. Yang, F. Bi, Y. Wang, J. Xu, N. Liu, Synthesis of acidic MIL-125 from plastic waste: significant contribution of N orbital for efficient photocatalytic degradation of chlorobenzene and toluene, Appl. Catal. B Environ. 310 (2022), 121300, https://doi.org/10.1016/j.apcatb.2022.121300.

[63] Z. Teng, Q. Zhang, H. Yang, K. Kato, W. Yang, Y. Lu6, S. Liu, C. Wang, A. Yamakata, C. Su, B. Liu, T. Ohno, Atomically dispersed antimony on carbon nitride for the artificial photosynthesis of hydrogen peroxide, Nat. Catal. 4 (2021) 374–384, https://doi.org/10.1038/s41929-021-00605-1.

[64] Y. Nosaka, A. Nosaka, Generation and detection of reactive oxygen species in photocatalysis, Chem. Rev. 117 (2017) 11302–11336, https://doi.org/10.1021/acs.chemrev.7b00161.

[65] Q. Li, J. Ren, Y. Hao, Y. Li, X. Wang, Y. Liu, R. Su, F. Li, Insight into reactive species-dependent photocatalytic toluene mineralization and deactivation pathways via modifying hydroxyl groups and oxygen vacancies on BiOCl, Appl. Catal. B Environ. 317 (2022), 121761, https://doi.org/10.1016/j.apcatb.2022.121761.

[66] J. Li, K. Li, B. Lei, M. Ran, Y. Sun, Y. Zhang, K. Kim, F. Dong, High-efficiency photocatalytic decomposition of toluene over defective InOOH: promotive role of oxygen vacancies in ring opening process, Chem. Eng. J. 413 (2021), 127389, https://doi.org/10.1016/j.cej.2020.127389.

[67] X. Dong, W. Cui, H. Wang, J. Li, Y. Sun, H. Wang, Y. Zhang, H. Huang, F. Dong, Promoting ring-opening efficiency for suppressing toxic intermediates during photocatalytic toluene degradation via surface oxygen vacancies, Sci. Bull. 64 (2019) 669–678, https://doi.org/10.1016/j.scib.2019.04.020.

[68] W. Cui, J. Li, L. Chen, X. Dong, H. Wang, J. Sheng, Y. Sun, Y. Zhou, F. Dong, Nature-inspired CaCO₃ loading TiO₂ composites for efficient and durable photocatalytic mineralization of gaseous toluene, Sci. Bull. 65 (2020) 1626–1634, https://doi.org/10.1016/j.scib.2020.05.024.

[69] K. Zhang, H. Chen, Y. Liu, J. Deng, L. Jing, A. Rastegarpanah, W. Pei, Z. Han, H. Dai, Two-dimensional Bi₂WₓMo₁₋ₓO₆ solid solution nanosheets for enhanced photocatalytic toluene oxidation to benzaldehyde, Appl. Catal. B Environ. 315 (2022), 121545, https://doi.org/10.1016/j.apcatb.2022.121545.

[70] J. Wang, J. Li, W. Yang, Y. Liu, H. Wang, Q. Geng, F. Dong, Promote reactants activation and key intermediates formation for facilitated toluene photodecomposition via Ba active sites construction, Appl. Catal. B Environ. 297 (2021), 120489, https://doi.org/10.1016/j.apcatb.2021.120489.

[71] W. He, J. Li, X. Hou, P. Chen, H. Wang, X. Dong, F. Dong, Y. Sun, Light-induced secondary hydroxyl defects in Sr₁₋ₓSn(OH)₆ enable sustained and efficient photocatalytic toluene mineralization, Chem. Eng. J. 427 (2022), 131764, https://doi.org/10.1016/j.cej.2021.131764.

[72] X. Yang, X. Yu, M. Jing, W. Song, J. Liu, M. Ge, Defective MnₓZr₁₋ₓO₂ solid solution for the catalytic oxidation of toluene: insights into the oxygen vacancy contribution, ACS Appl. Mater. Interfaces 11 (2019) 730–739, https://doi.org/10.1021/acsami.8b17062.

[73] J. Zhang, B. Shen, Z. Hu, M. Zhen, S. Guo, F. Dong, Uncovering the synergy between Mn substitution and O vacancy in ZnAl-LDH photocatalyst for efficient toluene removal, Appl. Catal. B Environ. 296 (2021), 120376, https://doi.org/10.1016/j.apcatb.2021.120376.

[74] L. Chen, W. Cui, J. Li, H. Wang, X. Dong, P. Chen, Y. Zhou, F. Dong, The high selectivity for benzoic acid formation on Ca₂Sb₂O₇ enables efficient and stable toluene mineralization, Appl. Catal. B Environ. 271 (2020), 118948, https://doi.org/10.1016/j.apcatb.2020.118948.

[75] B. Chen, P. Ouyang, Y. Li, Y. Duan, K. Lv, S. Carabineiro, F. Dong, Creation of an internal electric field in SnO₂@ZnS-ZnSn(OH)₆ dual-type-II heterojunctions for efficient NO photo-oxidation, Sci. China Mater. 66 (2023) 1447–1459, https://doi.org/10.1007/s40843-022-2288-0.

[76] W. Zhang, Y. Wang, Y. Wang, Y. Liang, F. Dong, Highly efficient photocatalytic NO removal and in situ DRIFTS investigation on SrSn(OH)₆, Chin. Chem. Lett. 33 (2022) 1259–1262, https://doi.org/10.1016/j.cclet.2021.07.065.

[77] J. Zhang, H. Tao, S. Wu, J. Yang, M. Zhu, Enhanced durability of nitric oxide removal on TiO₂ (P25) under visible light: enabled by the direct Z-scheme mechanism and enhanced structure defects through coupling with C3N5, Appl. Catal. B Environ. 296 (2021), 120372, https://doi.org/10.1016/j.apcatb.2021.120372.

[78] P. Zhang, Y. Huang, Y. Rao, M. Chen, X. Li, W. Ho, S. Lee, J. Cao, Chemical etching fabrication of uniform mesoporous Bi@Bi₂O₃ nanospheres with enhanced visible light-induced photocatalytic oxidation performance for NOₓ, Chem. Eng. J. 406 (2021), 126910, https://doi.org/10.1016/j.cej.2020.126910.

[79] Y. Duan, Y. Wang, L. Gan, J. Meng, Y. Feng, K. Wang, K. Zhou, C. Wang, X. Han, X. Zhou, Amorphous carbon nitride with three coordinate nitrogen (N₃C) vacancies for exceptional NOₓ abatement in visible light, Adv. Energy Mater. 11 (2021), 2004001, https://doi.org/10.1002/aenm.202004001.

[80] B. Lei, W. Cui, J. Sheng, H. Wang, P. Chen, J. Li, Y. Sun, F. Dong, Synergistic effects of crystal structure and oxygen vacancy on Bi₂O₃ polymorphs: intermediates activation, photocatalytic reaction efficiency, and conversion pathway, Sci. Bull. 65 (2020) 467–476, https://doi.org/10.1016/j.scib.2020.01.007.